

**Laser-induced cavitation in liquid  $^4\text{He}$  near the liquid-vapor critical point**Kenneth R. Langley <sup>1,\*</sup>, Tariq Alghamdi <sup>2,\*</sup>, Andres A. Aguirre-Pablo <sup>1</sup>, Nathan B. Speirs <sup>1,3</sup>,  
S. T. Thoroddsen <sup>1</sup> and Peter Taborek<sup>4,†</sup><sup>1</sup>*Division of Physical Science and Engineering, King Abdullah University of Science and Technology (KAUST), Thuwal 23955-6900, Saudi Arabia*<sup>2</sup>*Mechanical Engineering Department, College of Engineering and Architecture, Umm Al-Qura University, Makkah 21955, Saudi Arabia*<sup>3</sup>*Department of Mechanical Engineering, Brigham Young University, Provo, Utah 84602, USA*<sup>4</sup>*Department of Physics and Astronomy, University of California–Irvine, Irvine, California 92697, USA*

(Received 25 April 2024; accepted 28 August 2024; published 9 September 2024)

High-speed videos in an optical cryostat, with frame rates up to  $5 \times 10^6$  fps, are used to study the dynamics of laser-induced cavitation in helium near the critical point and in the supercritical region. The propagation of strong shock waves are observed in both regimes. The time dependence of the cavitation bubble radius as well as the acoustic pressure field outside the bubble are described by standard compressible flow models. In the temperature range  $4K < T < 5.2K$ , a symmetric cloud of micron-scale bubbles are observed outside the main cavitation bubble as it approaches its maximum radius which is due to homogeneous nucleation and spinodal decomposition in the low-pressure fluid outside the bubble. Nucleation of secondary bubbles is also observed far below the critical point, but this requires large negative pressures that can be generated by shock waves that reflect from the primary bubble.

DOI: [10.1103/PhysRevFluids.9.L091601](https://doi.org/10.1103/PhysRevFluids.9.L091601)

*Introduction.* Cavitation occurs when a liquid is rapidly driven out of equilibrium, either by superheating or depressurization, which causes a vapor bubble to nucleate and grow and eventually collapse. Cavitation is an important issue in supercritical materials science studies [1], in pumping systems for cryogenic rocket propellants [2], and in power cycles utilizing working fluids near the critical point [3–6]. Transient depressurization can occur in nozzle flows [7,8] or in high-intensity acoustic waves [9–12]. Cavitation can be conveniently studied by locally superheating a small region of fluid using electrical heaters [13,14] or by focusing a pulsed laser into bulk fluid, which is the technique used herein. The highly nonlinear process following the focused laser pulse leads to dielectric breakdown and transient high-pressure plasma formation in the liquid, as discussed in Refs. [15–17]. Most previous studies, which utilize imaging to study the subsequent bubble dynamics of laser-induced cavitation, have used water or aqueous media as the working fluid [18–24]. There are several reasons why helium is an interesting fluid for cavitation studies. It is extremely chemically pure, so there are no complications associated with dissolved noncondensable gas or heterogeneous nucleation sites, which makes quantitative comparison to predictions of simple models feasible [9]. The entire coexistence range of the liquid-vapor phase transition is experimentally accessible, as in the narrow temperature range from 1 to 5 K, one spans from the low-temperature regime with vanishing vapor pressure to the critical point where the compressibility

\*These authors contributed equally to this work.

†Contact author: [ptaborek@uci.edu](mailto:ptaborek@uci.edu)

diverges and the density difference between liquid and vapor and the surface tension both approach zero. Similarly, since the critical pressure is so low ( $\simeq 2$  bars), it is not difficult to explore the supercritical single phase region. In contrast, the critical point for water occurs at 220 atm and 374 °C, making imaging experiments challenging.

Several previous studies of cavitation in liquid helium at low temperatures have used high-intensity ultrasound [9,25–27] to induce cavitation but only using single point detectors to provide qualitative information about bubble dynamics. A few more recent works have used time-lapse stroboscopic imaging of acoustically generated cavitation [28] and laser ablation of metal targets under liquid helium [29,30], but none near the critical point.

*Experimental setup.* We utilize high-speed video imaging to capture the full dynamics of laser-induced cavitation bubbles in liquid helium-4 above and below the liquid-vapor critical point at  $T_{\text{crit}} = 5.19$  K,  $P_{\text{crit}} = 200.2$  kPa. Experiments were performed in a custom-built optical cryostat, which has been described previously [31–33]. The experimental cell consists of a 71-mm per edge cube of gold-plated copper with 38-mm-diameter bores drilled through each face except the top of the cell. The cell is equipped with sapphire windows with indium gaskets to provide optical access to its interior. Helium (99.999% pure) was liquified directly in the experimental cell until the cell was full of liquid. For measurements below the critical pressure, the experimental cell is kept at saturation conditions, so the ambient pressure at the point of cavitation,  $P_{\infty}$ , is the saturated vapor pressure at the cell temperature,  $P_{\text{sat}}(T)$ . For measurements in the supercritical regime, the pressure was set by the gas pressure in the helium fill line. The thermophysical and transport properties of helium used herein were compiled from data provided in the literature [34,35].

Laser pulses, 6 ns in duration, were generated using a Litron Nano PIV L200-15, Nd:YAG laser at wavelength 532 nm. The laser beam is initially expanded and then passes through the various sapphire windows in the vacuum chamber/radiation shields into the test cell. The beam is focused using a parabolic mirror inside the liquid in the cell resulting in a beam waist diameter of approximately 150  $\mu\text{m}$ . The pulse rate was less than one pulse/5 min.

Images of the cavitation event were captured using a Kirana-05M ultrahigh-speed video camera (Specialised Imaging, Pitstone, UK) at frame rates between 2000 and  $5 \times 10^6$  fps back-illuminated by a pulsed laser diode with a pulse duration between 20 and 170 ns. This camera captures 180 frames with an image size of  $924 \times 768$  pixels regardless of frame rate. Separately, a Phantom v2511 CMOS camera was used to image the event at frame rates between 33 and 380 kfps with image size decreasing with increasing frame rate. The cameras were coupled to a Questar QM1 long-distance microscope resulting in image resolution between 5.66 and 45  $\mu\text{m}/\text{pixel}$  depending on configuration.

*Theoretical considerations.* The basic cavitation phenomena we observe are illustrated in Fig. 1, which shows backlit images of cavitation bubbles in liquid near the critical point at saturated vapor pressure (top row) and at approximately the same temperature, but higher pressure (bottom row). At short times an outgoing shock wave is visible. Away from the critical point at higher pressure, the bubble expands and contracts, always maintaining a sharp interface between liquid and vapor. In contrast, bubbles generated at coexistence develop a fuzzy boundary once they reach their maximum radius, which is due to nucleation of microscopic secondary bubbles driven by the acoustic field of the primary bubble. The formation of these microbubbles is clearly visible in the high magnification videos in the Supplemental Material [36]. The main purpose of this Letter is to document this universal aspect of bubble dynamics near the critical point and to provide a theoretical basis for understanding it. Such experiments have not been conducted near the critical point in water.

The velocity potential for potential flow of an ideal incompressible fluid obeys the Laplace equation, which is the basis of the Rayleigh-Plesset equation of bubble dynamics. Taking compressibility into account at first order requires solving the wave equation instead. Various methods of approximating the solution to the wave equation with moving boundaries have been analyzed in the literature [37] which result in equations of motion that have slightly different terms but are numerically indistinguishable; we have used an equation derived by Keller and collaborators

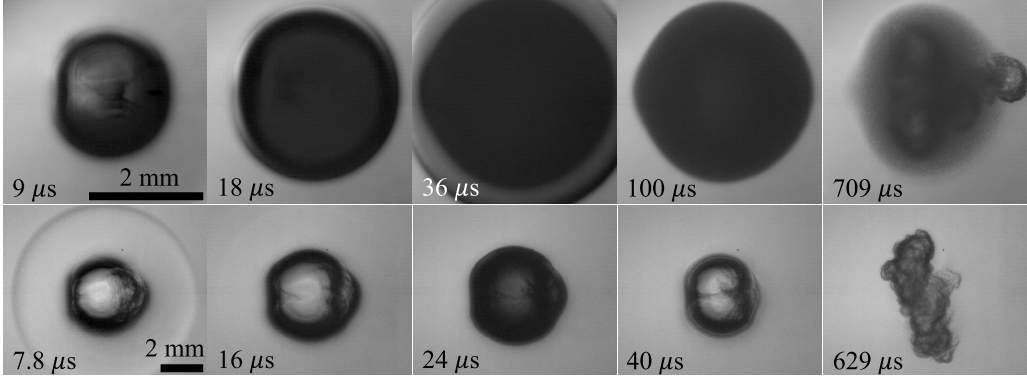


FIG. 1. Snapshots of bubble dynamics from high-speed videos. Top row shows a cavitation bubble at  $T = 5.02$  K and  $P = 199$  kPa, close to the critical point; note the symmetric shell of tiny bubbles that nucleate around the main bubble. The bottom row shows a bubble at  $T = 4.97$ , but at  $P = 383$  kPa, far from the coexistence curve and the critical point. Videos are available at [36].

[38,39]:

$$R''(t)R(t)\left(1 - \frac{R'(t)}{c}\right) + \frac{3}{2}R'(t)^2\left(1 - \frac{R'(t)}{3c}\right) = \frac{1}{\rho}\left(\frac{P_0R_0^5}{R(t)^5} - P_\infty\right)\left(1 + \frac{R'(t)}{c}\right) - \frac{5P_0R_0^5R'(t)}{c\rho R(t)^5}, \quad (1)$$

where  $R(t)$  is the bubble radius as a function of time,  $c$  is the (constant) speed of sound in the liquid,  $P_\infty$  is the pressure far from the bubble, and  $\rho$  is the density of the background fluid; surface tension and viscous terms have been omitted because they were confirmed to be negligible. The interior of the bubble is modeled as an ideal gas, with initial pressure  $P_0$  and radius  $R_0$ . Since heat transfer is neglected,  $PV^{5/3} \propto PR^5$  is constant, so the pressure inside the bubble at later times is  $P_0 \times [R_0/R(t)]^5$ .

Equation (1) can be solved numerically with the initial conditions  $R(0) = R_0$  and  $R'(t) = 0$ ;  $P_0$  and  $R_0$  are treated as fitting parameters to qualitatively reproduce the experimentally observed maximum bubble radius and oscillation period. Typical results for  $R(t)$  and  $P(t)$  for a case with  $T = 4.3$  K are shown in Fig. 2. Note that when the bubble is near its maximum radius, the internal pressure is below  $P_\infty$ .

The oscillating bubble radiates sound into the background compressible fluid [40]. The pressure in the fluid  $P_L(r, t)$  is given by derivatives of the volume of the bubble,  $V(t) = 4\pi R(t)^3/3$  [38,41], evaluated at the retarded time  $t - r/c$ :

$$P_L(r, t) = P_\infty + \rho \left[ \frac{V''(t - \frac{r}{c})}{4\pi r} - \frac{V'^2(t - \frac{r}{c})}{32\pi^2 r^4} \right]. \quad (2)$$

Plots of  $P_L(r, t)$  in the fluid outside the bubble as a function of the radial coordinate  $r$  for several values of  $t$  are shown in Fig. 2(c). An important consequence of Eqs. (1) and (2) illustrated in Fig. 2 is that when the internal bubble pressure is below  $P_{\text{sat}}$ , there is also a region in the fluid outside the bubble with  $P_L(r, t) < P_{\text{sat}}$ , which means that the fluid is metastable.

The metastable liquid outside the cavitation bubble can undergo homogeneous nucleation of secondary vapor bubbles if the nucleation rate is sufficiently high. These secondary bubbles become visible in our experiments when the nucleation rate exceeds  $\sim 10^{20} \text{ m}^{-3} \text{ s}^{-1}$ . This rate corresponds to one nucleation inside a  $20 \mu\text{m}$  cube about every microsecond.

A quantitative estimate of the nucleation rate is based on the probability of forming a critical vapor nucleus that is sufficiently large that subsequent growth leads to a decrease in the free energy,

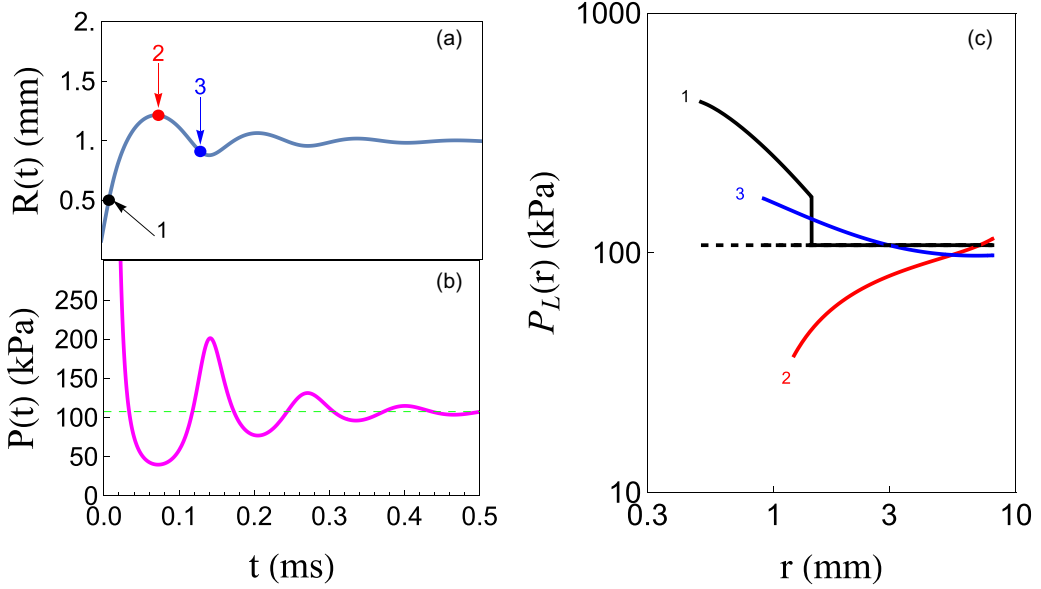


FIG. 2. (a) and (b) Results for the bubble radius  $R(t)$  and the bubble pressure  $P(t)$  as a function of time and computed from the Keller equation (1) for the case  $T_{\text{amb}} = 4.3$  K,  $P_0 = 8.1 \times 10^8$  Pa,  $R_0 = 2.4 \times 10^{-4}$  m,  $P_\infty = P_{\text{sat}} = 1.07 \times 10^5$  Pa. The numbers and symbols mark the times at which the pressure in the liquid  $P_L$  is shown in (c). The horizontal dashed line in (b) is the saturated vapor pressure. Note that for a significant fraction of the bubble life cycle, the internal pressure is below the saturated vapor pressure. (c) Log-log plots of the pressure in the exterior fluid  $P_L(r, t)$  as a function of  $r$  (the distance to the center of the bubble) for several values of  $t$  which correspond to the numbers and colors of the indicators in (a). The dashed horizontal line is  $P_\infty$ , which is often equal to  $P_{\text{sat}}$ . For a given  $t$ , the  $P_L(r, t)$  curve starts at the surface of the bubble where  $r = R(t)$ , which is marked by a number that corresponds to the bubble radius at a time indicated in (a).  $P_L(r, t) = P_\infty$  for  $r > ct$ , and has a shocklike singularity at  $r = ct$ . Note that when the bubble is near its maximum radius (case 2),  $P_L(r, t)$  is substantially lower than  $P_\infty$  over a spatial region that extends several bubble radii from the bubble wall.

which is the sum of a negative volume term that scales as  $r^3$  and a positive surface term that scales as  $r^2$ . The critical radius  $r_c$  is [9,42]

$$r_c = \frac{2\sigma}{(P_{\text{sat}} - P_L)\delta}, \quad (3)$$

where  $P_L$  is the pressure in the fluid and  $\delta$  is

$$\delta = 1 - \frac{n_v}{n_L} + \frac{1}{2} \left( \frac{n_v}{n_L} \right)^2, \quad (4)$$

where  $n_L$  and  $n_v$  are number densities in the liquid and vapor, respectively. The free-energy barrier to nucleation is

$$\Delta G(r_c) = \frac{4\pi r_c^3 (P_{\text{sat}} - P_L)}{6} \quad (5)$$

and the nucleation rate  $J$  is

$$J = n_L \left( \frac{2\sigma}{\pi m} \right)^{1/2} \exp \left( -\frac{\Delta G(r_c)}{kT} \right), \quad (6)$$

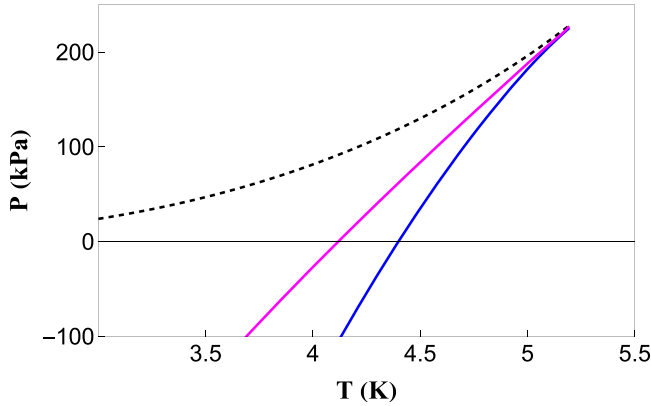


FIG. 3. Plots of characteristic pressures of liquid helium as a function of temperature near the critical point. The upper dashed black curve is the saturated vapor pressure. The lower blue curve is the spinodal line. On the spinodal, the compressibility goes to zero, and the region below it is experimentally inaccessible because the liquid is mechanically unstable. In the region between these two curves, the liquid is metastable, and bubbles will nucleate at a rate that is exponentially dependent on the degree of subpressure. The magenta curve corresponds to a nucleation rate of  $10^{20} \text{ m}^{-3} \text{ s}^{-1}$ . All three curves meet near the critical point, with  $P \sim 220 \text{ kPa}$  and  $T \sim 5.2 \text{ K}$ .

where  $m$  is the mass of a helium atom and  $k$  is Boltzmann's constant. We have used Eq. (6) together with the NIST thermophysical property tables [35] to compute the values of  $P_L$  as a function of  $T$ , which yield  $J \sim 10^{20} \text{ m}^{-3} \text{ s}^{-1}$ ; the results are shown as the magenta curve in Fig. 3. Figure 3 also shows the spinodal curve, shown in blue, which represents the locus of points where the compressibility (calculated from a van der Waals equation of state) of the liquid goes to zero. The spinodal is a boundary below which the metastable liquid becomes mechanically unstable.

*Results.* Although cavitation in liquids typically requires negative pressures [25], Fig. 3 shows that for  $^4\text{He}$  at  $T > 4 \text{ K}$ , pressures below the vapor pressure but above zero will lead to very high nucleation rates. Qualitatively, this is due to the strong dependence of the free-energy barrier on the liquid-vapor interfacial tension  $\sigma$ . Since  $\sigma$  goes to zero near the critical point, even small under pressures can generate large nucleation rates in the critical region. A sequence of images of the cavitation bubble for  $T = 5.03 \text{ K}$  together with plots of the pressure field in the surrounding fluid are shown in Fig. 4. As the main bubble approaches its maximum radius, the pressure in the surrounding fluid is below  $P_{\text{sat}}$  and a halo of tiny bubbles is nucleated outside the main bubble. When the main bubble starts to contract, the external pressure rises above  $P_{\text{sat}}$  and the halo mostly disappears, but returns when the main bubble starts expanding again. This phenomenon occurs only near the critical point; images of cavitation bubbles on the coexistence curve with  $T < 4 \text{ K}$  shown in Fig. 5 or at higher temperatures but with  $P_{\infty} > P_{\text{sat}}$  (as shown in Fig. 1, bottom row) have sharp boundaries.

An important feature of the short-time dynamics of cavitation is the emission of a spherical shock wave. These shock waves are visible in the images such as Figs. 5(a) and 5(c) because the high pressures at the leading edge of the shock increases the density and optical index of the fluid. For  $1 < t < 10 \mu\text{s}$ , the time dependence of the radius of the shock front  $r_s$  can be accurately described by a power law  $r_s \sim t^n$  where  $0.6 < n < 0.9$ . The velocity of the shock  $v_s$  can be obtained by differentiation. The density  $\rho_s$  and pressure  $P_s$  at the shock front can be determined from the conservation of mass and momentum equations [29]:

$$\rho_s(v_s - v_p) = \rho v_s, \quad P_s + \rho_s(v_s - v_p)^2 = P_{\infty} + \rho v_s^2, \quad (7)$$

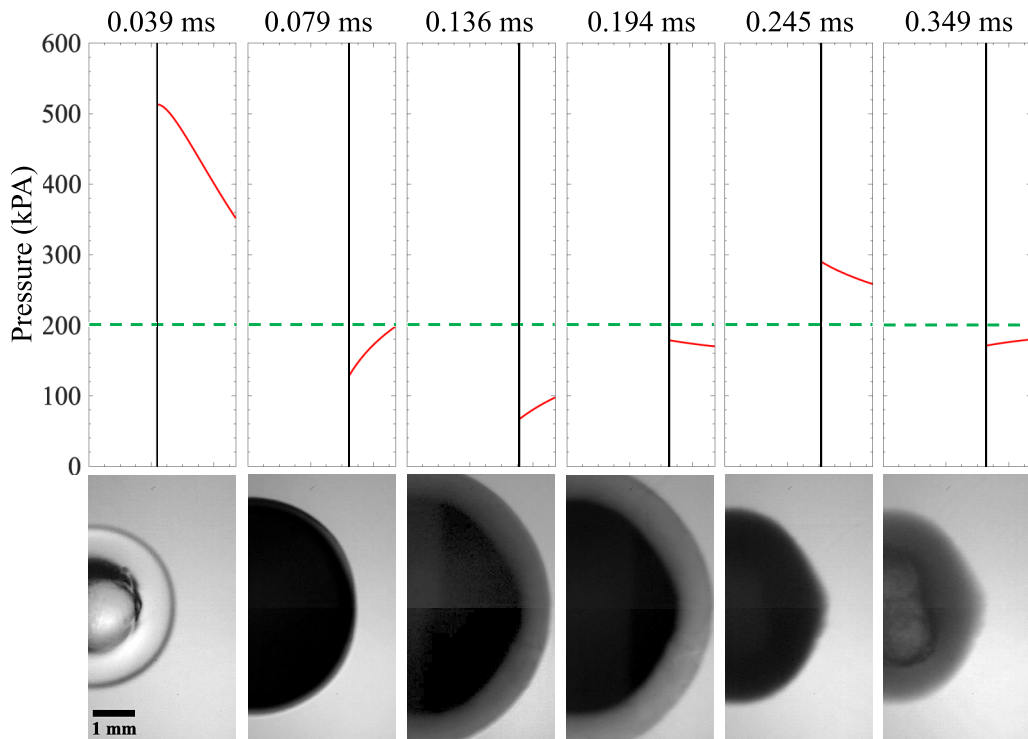


FIG. 4. Cavitation in  ${}^4\text{He}$  at  $T = 5.03$  K with  $P_\infty = P_{\text{sat}}$ . The lower panel shows backlit transmission images of the bubble for several times that span the range of the initial expansion and the first contraction. The upper panel shows the pressure  $P_L(r, t)$  as a function of  $r$  outside the bubble calculated using Eq. (2). The vertical lines mark  $R(t)$  computed from Eq. (1) and the green-dashed horizontal line is the saturated vapor pressure. The first image at  $t = 0.039$  ms shows a central bubble with a detached shock wave. In subsequent images, the central main bubble appears very dark. The images at  $t = 0.136$ ,  $0.194$ , and  $0.349$  ms also have a shell of tiny ( $\approx 1$  pixel) bubbles that appear as a gray ring around the main bubble. As indicated by the pressure graph above these images, the halo of small bubbles occurs when the pressure in the external fluid is below the saturated vapor pressure. When the pressure rises again above  $P_{\text{sat}}$  (e.g., at  $t = 0.245$  and  $0.405$  ms), the halo abruptly disappears. The complete video is available at [36].

where  $v_p$  is the velocity of the piston driving the shock. These equations together with an empirical linear relation [29] between  $v_s$  and  $v_p$ ,

$$v_p = c_1 (v_s - c), \quad (8)$$

can be solved for  $P_s$ :

$$P_s = P_\infty + c_1 v_s (v_s - c) \rho. \quad (9)$$

The values of  $P_s$  determined in this way using  $c_1 = 0.735$  are shown in Fig. 6(b).

In the two-phase region with  $T < T_c$ , an expanding core of hot high-pressure gas drives the shock wave in the surrounding liquid. In the supercritical regime, a conventional cavitation bubble cannot form because there is only a single phase with a continuous variation of the density. The rapid localized heating from the laser pulse nevertheless causes thermal expansion, which creates a spherical piston and launches a shock wave with characteristics similar to those generated at lower temperatures, as shown in Fig. 6. The subsequent dynamics of the “bubble” is quite different in the two cases. In the supercritical case, the hot fluid is initially localized in a region defined by the focus

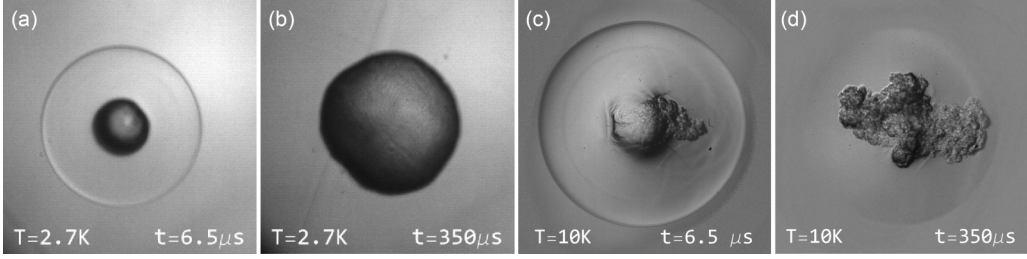


FIG. 5. Behavior of cavitation bubbles above and below the critical region. Images (a) and (b) in the left-hand column were obtained on the two-phase coexistence curve with  $T = 2.7$  K. Images (c) and (d) on the right-hand column were obtained in the supercritical region, with  $T = 10$  K and  $P = 2 \times 10^6$  Pa;  $t$  is the time after the laser pulse. The width of each of the images is 7.5 mm: (a) shows a dark spherical bubble with a diameter  $\approx 1$  mm, and a concentric clear disk, which is an  $\text{Ma} = 1.3$  shock wave. A similar shock wave with  $\text{Ma} = 2.9$  is generated in the supercritical fluid, shown in (c), but the central core of hot fluid has a less well-defined boundary. At later times in the two-phase region, the vapor bubble has increased its diameter, but retains a compact near-spherical shape shown in (b), while in the supercritical fluid, the turbulent mixing of the hot fluid and the absence of stabilizing surface tension leads to an irregular shape, shown in (d). Videos are available at [36].

of the laser ( $\approx 150 \mu\text{m}$ ), but then turbulent motion mixes the fluid into a region of characteristic scale  $\approx 1$  mm within 1 ms. The blob of hot fluid remains visible and retains its structure with a reasonably well-defined interface with the colder background fluid for our maximum observation period of hundreds of milliseconds. This is consistent with the fact that the thermal diffusivity  $\chi$  of helium in the near supercritical regime is  $\chi \approx 10^{-7} \text{ m}^2/\text{s}$  so the expected thermal relaxation time  $\tau = L^2/\chi$  for  $L = 1$  mm is  $\sim 10$  s.

The shock wave launches within the first microsecond of the initial plasma formation and propagates across the experimental cell and eventually reflects from the walls, returning hundreds of microseconds later to interact with the (now much larger) bubble. When the initial positive pressure shock reflects from the high acoustic impedance of the metallic cell walls, the reflected pulse is also a positive pressure shock. In contrast, when the positive pressure shock reflects from a low impedance boundary such as a free vapor surface or the interior of a vapor bubble, the polarity of the pressure is reversed [22,43,44]. This negative pressure generated by a reflected shock can induce nucleation of secondary bubbles even at temperatures far below the critical point as shown in Fig. 7.

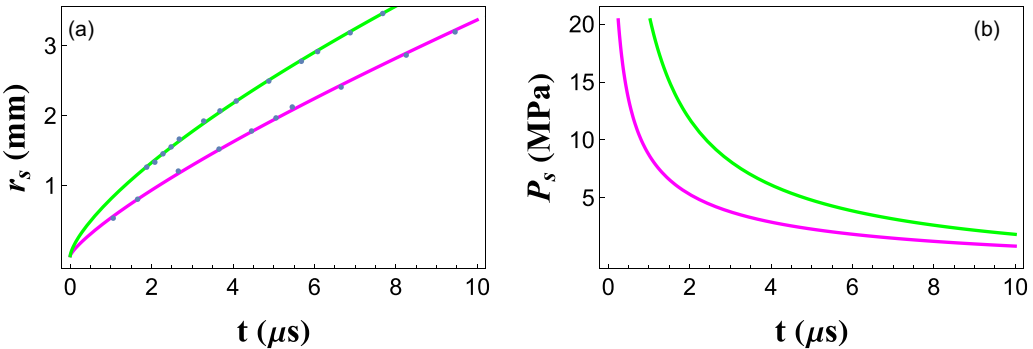


FIG. 6. (a) Shock radius  $r_s$  as a function of time after the laser pulse. Green curve corresponds to  $T = 10$  K and  $P_\infty = 2$  MPa. Magenta curve corresponds to  $T = 2.72$  K and  $P_\infty = 0.1$  MPa. Points are extracted from videos. Green curve is a power-law fit with  $r_s \sim t^{0.71}$  and magenta curve is a fit with  $r_s \sim t^{0.79}$ . (b) Shock pressure  $P_s$  as a function of time calculated from the data in (a) and Eq. (9).

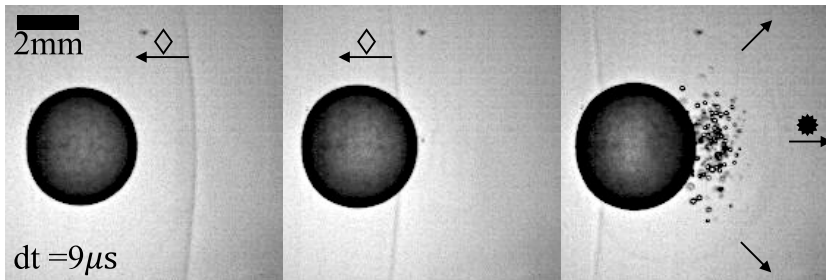


FIG. 7. Three frames from a video showing a positive pressure nearly vertical linear shock ( $\diamond$ ) propagating from right to left interacting with an expanding cavitation bubble at  $T = 2.24$  K with  $P_\infty = 5.8$  kPa. The last frame shows nucleation of secondary bubbles due to the negative pressure generated by the shock reflecting from the main bubble (\*). The complete video is available at [36].

The figure shows an essentially planar positive pressure reflected shock moving from right to left with a velocity of 263 m/s. Using Eq. (9) with  $c = 221$  m/s, the peak pressure is approximately 1 MPa, so the reflected shock will have a pressure of  $\sim -1$  MPa. From Eq. (6), the negative pressure required for  $J \sim 10^{20}$  is  $-0.5$  MPa, which is consistent with the strong nucleation we observe on one side of the main bubble, behind the reflected shock.

*Conclusions.* Taking the compressibility of the background fluid into account is important for understanding the qualitative behavior of cavitation near the critical point. As the bubble radius reaches its maximum value, the internal bubble pressure and the pressure in the adjacent fluid typically drops below the saturated vapor pressure. The acoustic wave that is generated has a wavelength that is typically several millimeters, so there is a significant region of depressurized liquid surrounding the vapor bubble. Near the critical point, the liquid pressure approaches the spinodal pressure and there is rapid homogeneous nucleation of microscopic vapor bubbles in a spherical shell around the cavitation bubble, which appears as a gray fog in the video images, but become distinct at larger magnification (see Supplemental Material [36]). As the main cavitation bubble begins to collapse, the pressure around it rises to above the saturation vapor pressure and most of the tiny bubbles recondense. The thermodynamic properties of a fluid near the critical point obey well-known scaling laws, so these results should be applicable to a wide range of fluids, including recent studies of laser ablation in near critical  $\text{CO}_2$  [45]. Our results clarify the nature of the observed *double layer* observed in their snapshots.

In the single-phase supercritical region, the energy deposited by the laser pulse causes rapid thermal expansion and launches a shock wave that is particularly strong because of the high compressibility and low speed of sound. The subsequent dynamics of the fluid is distinctly different from vapor bubbles generated below the critical point: since there is no stored elastic energy, there are no oscillations and the thermal energy is slowly transported by turbulent convection and diffusion.

Secondary bubbles around the main cavitation bubble can be nucleated by shock waves even at temperatures far below the critical temperature (Fig. 7), but the phenomenon and the mechanism are distinctly different from the near critical case. The large negative pressures required to induce nucleation at low temperatures can be generated by positive pressure shock waves that reflect from the bubble as negative pressure shocks that produce an asymmetric distribution of secondary bubbles. Such shock-induced secondary bubbles have been observed in other liquids, including water [22,43,46,47], but experimental values of the tension (negative pressure) needed for homogeneous nucleation in bulk water are typically in the range of  $-20$  to  $-60$  MPa, which is much smaller than the value of  $-140$  MPa predicted by classical theory [48]. The presence of nanobubbles and solid impurities therefore play a dominant role for cavitation in bulk water. In contrast, nucleation rate measurements using liquid helium, which is free of dissolved gas and impurities, yield results in

close correspondence with classical theory [49]. The experiments using pure helium reported here thus provide a useful benchmark for future work and an opportunity for meaningful confrontation with theoretical models of pressure wave-induced nucleation of bubbles.

*Acknowledgment.* This research was funded by King Abdullah University of Science and Technology (KAUST) under Grants No. URF/1/4075-01-01 and No. BAS/1/1352-01-01.

- 
- [1] K. Urabe, T. Kato, S. Stauss, S. Himeno, S. Kato, H. Muneoka, M. Baba, T. Suemoto, and K. Terashima, Dynamics of pulsed laser ablation in high-density carbon dioxide including supercritical fluid state, *J. Appl. Phys.* **114**, 143303 (2013).
  - [2] M. Dular and M. Petkovsek, Cavitation erosion in liquid nitrogen, *Wear* **400-401**, 111 (2018).
  - [3] H. S. Pham, N. Alpy, S. Mensah, M. Tothill, J. H. Ferrasse, O. Boutin, J. Quenaut, G. Rodriguez, and M. Saez, A numerical study of cavitation and bubble dynamics in liquid  $\text{CO}_2$  near the critical point, *Int. J. Heat Mass Transfer* **102**, 174 (2016).
  - [4] S. Banik, S. Ray, and S. De, Thermodynamic modelling of a recompression  $\text{CO}_2$  power cycle for low temperature waste heat recovery, *Appl. Therm. Eng.* **107**, 441 (2016).
  - [5] Y. Liu, Y. Zhao, Q. Yang, G. Liu, and L. Li, Thermodynamic comparison of  $\text{CO}_2$  power cycles and their compression processes, *Case Stud. Therm. Eng.* **21**, 100712 (2020).
  - [6] W. Xie, Y. Tian, P. Jiang, B. Wang, and X. Xu, Effects of near-critical condensation and cavitation on the performance of S- $\text{CO}_2$  compressor, *Energies* **17**, en17040854 (2024).
  - [7] T. Ishii and M. Murakami, Comparison of cavitation flows in He I and He II, *Cryogenics* **43**, 507 (2003).
  - [8] K. Ohira, T. Nakayama, and T. Nagai, Cavitation flow instability of subcooled liquid nitrogen in converging-diverging nozzles, *Cryogenics* **52**, 35 (2012).
  - [9] H. J. Maris, S. Balibar, and M. S. Pettersen, Nucleation of bubbles in liquid-helium, *J. Low Temp. Phys.* **93**, 1069 (1993).
  - [10] M. Ashokkumar, The characterization of acoustic cavitation bubbles—an overview, *Ultrason. Sonochem.* **18**, 864 (2011).
  - [11] P. Roche, H. Lambaré, E. Rolley, D. Lacoste, S. Balibar, C. Guthmann, and H. Maris, Growth and collapse of bubbles in superfluid  $^4\text{He}$ , *Czech. J. Phys.* **46**, 381 (1996).
  - [12] A. Žnidarčič, R. Mettin, and M. Dular, Modeling cavitation in a rapidly changing pressure field—application to a small ultrasonic horn, *Ultrason. Sonochem.* **22**, 482 (2015).
  - [13] V. E. Vinogradov, P. A. Pavlov, and V. G. Baidakov, Explosive cavitation in superheated liquid argon, *J. Chem. Phys.* **128**, 234508 (2008).
  - [14] V. G. Baidakov, V. E. Vinogradov, and P. A. Pavlov, Spontaneous cavitation in liquid n-butane at negative and positive pressures, *Int. J. Heat Mass Transfer* **111**, 624 (2017).
  - [15] G. Winterling, W. Heinicke, and K. Dransfeld, Laser-induced breakdown in liquid  $\text{He}^4$ , *Phys. Rev.* **185**, 285 (1969).
  - [16] S. Brueck and H. Kildal, Laser-induced dielectric-breakdown in cryogenic liquids, *J. Appl. Phys.* **52**, 1004 (1981).
  - [17] S. Sirisky, Y. Yang, W. Wei, and H. Maris, Laser-induced breakdown in liquid helium, *J. Low Temp. Phys.* **189**, 53 (2017).
  - [18] A. Vogel, S. Busch, and U. Parlitz, Shock wave emission and cavitation bubble generation by picosecond and nanosecond optical breakdown in water, *J. Acoust. Soc. Am.* **100**, 148 (1996).
  - [19] P. Robinson, J. Blake, T. Kodama, A. Shima, and Y. Tomita, Interaction of cavitation bubbles with a free surface, *J. Appl. Phys.* **89**, 8225 (2001).
  - [20] O. Lindau and W. Lauterborn, Cinematographic observation of the collapse and rebound of a laser-produced cavitation bubble near a wall, *J. Fluid Mech.* **479**, 327 (2003).
  - [21] C.-D. Ohl, M. Arora, R. Dijkink, V. Janve, and D. Lohse, Surface cleaning from laser-induced cavitation bubbles, *Appl. Phys. Lett.* **89**, 074102 (2006).

- [22] K. Ando, A.-Q. Liu, and C.-D. Ohl, Homogeneous nucleation in water in microfluidic channels, *Phys. Rev. Lett.* **109**, 044501 (2012).
- [23] X. Lyu, S. Pan, X. Hu, and N. A. Adams, Numerical investigation of homogeneous cavitation nucleation in a microchannel, *Phys. Rev. Fluids* **3**, 064303 (2018).
- [24] O. Supponen, D. Obreschkow, and M. Farhat, Rebounds of deformed cavitation bubbles, *Phys. Rev. Fluids* **3**, 103604 (2018).
- [25] J. A. Nissen, E. Bodegom, L. C. Brodie, and J. S. Semura, Tensile-strength of liquid  $^4\text{He}$ , *Phys. Rev. B* **40**, 6617 (1989).
- [26] H. Lambare, P. Roche, S. Balibar, H. Maris, O. Andreeva, C. Guthmann, K. Keshishev, and E. Rolley, Cavitation in superfluid helium-4 at low temperature, *Eur. Phys. J. B* **2**, 381 (1998).
- [27] S. Balibar, Nucleation in quantum liquids, *J. Low Temp. Phys.* **129**, 363 (2002).
- [28] A. Qu, A. Trimeche, P. Jacquier, and J. Grucker, Dramatic effect of superfluidity on the collapse of  $^4\text{He}$  vapor bubbles, *Phys. Rev. B* **93**, 174521 (2016).
- [29] A. Garcia, X. Buelna, E. Popov, and J. Eloranta, Time-resolved study of laser initiated shock wave propagation in superfluid  $^4\text{He}$ , *J. Chem. Phys.* **145**, 124504 (2016).
- [30] X. Buelna, E. Popov, and J. Eloranta, Dynamics of laser ablation in superfluid  $^4\text{He}$ , *J. Low Temp. Phys.* **186**, 197 (2017).
- [31] N. B. Speirs, K. R. Langley, P. Taborek, and S. T. Thoroddsen, Jet breakup in superfluid and normal liquid  $^4\text{He}$ , *Phys. Rev. Fluids* **5**, 044001 (2020).
- [32] D. Mallin, K. R. Langley, A. A. Aguirre-Pablo, M. L. Wallace, M. Milgie, S. T. Thoroddsen, and P. Taborek, Spreading of normal liquid helium drops, *Phys. Rev. E* **102**, 043105 (2020).
- [33] M. L. Wallace, D. Mallin, M. Milgie, A. A. Aguirre-Pablo, K. R. Langley, S. T. Thoroddsen, and P. Taborek, Impact and lifecycle of superfluid helium drops on a solid surface, *Phys. Rev. Fluids* **5**, 093602 (2020).
- [34] R. J. Donnelly and C. F. Barenghi, The observed properties of liquid helium at the saturated vapor pressure, *J. Phys. Chem. Ref. Data* **27**, 1217 (1998).
- [35] E. W. Lemmon, M. O. McLinden, and D. G. Friend, Thermophysical properties of fluid systems, in *NIST Chemistry WebBook, NIST Standard Reference Database Number 69*, edited by P. J. Linstrom and W. G. Mallard (National Institute of Standards and Technology, Gaithersburg, MD, 2019).
- [36] See Supplemental Material at <http://link.aps.org/supplemental/10.1103/PhysRevFluids.9.L091601> for videos.
- [37] A. Prosperetti and A. Lezzi, Bubble dynamics in a compressible liquid. Part 1. First-order theory, *J. Fluid Mech.* **168**, 457 (1986).
- [38] J. B. Keller and I. Kolodner, Damping of underwater explosion bubble oscillations, *J. Appl. Phys.* **27**, 1152 (1956).
- [39] J. Keller and M. Miksis, Bubble oscillations of large amplitude, *J. Acoust. Soc. Am.* **68**, 628 (1980).
- [40] S. R. Gonzalez-Avila, F. Denner, and C.-D. Ohl, The acoustic pressure generated by the cavitation bubble expansion and collapse near a rigid wall, *Phys. Fluids* **33**, 032118 (2021).
- [41] L. Landau and E. Lifshitz, *Fluid Mechanics: Landau and Lifshitz: Course of Theoretical Physics* (Elsevier Science, Amsterdam, 2013), Vol. 6.
- [42] J. Diemand, R. Angelil, K. K. Tanaka, and H. Tanaka, Direct simulations of homogeneous bubble nucleation: Agreement with classical nucleation theory and no local hot spots, *Phys. Rev. E* **90**, 052407 (2014).
- [43] P. A. Quinto-Su and K. Ando, Nucleating bubble clouds with a pair of laser-induced shocks and bubbles, *J. Fluid Mech.* **733**, R3 (2013).
- [44] N. B. Speirs, K. R. Langley, T. T. Pan, Z. Truscott, and S. T. Thoroddsen, Cavitation in the early moments of low-speed solid-liquid impact, *Nat. Commun.* **12**, 7250 (2021).
- [45] H. Muneoka, S. Himeno, K. Urabe, S. Stauss, M. Baba, T. Suemoto, and K. Terashima, Dynamics of cavitation bubbles formed by pulsed-laser ablation plasmas near the critical point of  $\text{CO}_2$ , *J. Phys. D: Appl. Phys.* **52**, 025201 (2019).
- [46] D. Obreschkow, N. Dorsaz, P. Kobel, A. de Bosset, M. Tinguely, J. Field, and M. Farhat, Confined shocks inside isolated liquid volumes: A new path of erosion? *Phys. Fluids* **23**, 101702 (2011).

- [47] S. Sembian, M. Liverts, N. Tillmark, and N. Apazidis, Plane shock wave interaction with a cylindrical water column, [Phys. Fluids \*\*28\*\*, 056102 \(2016\)](#).
- [48] E. Herbert, S. Balibar, and F. Caupin, Cavitation pressure in water, [Phys. Rev. E \*\*74\*\*, 041603 \(2006\)](#).
- [49] F. Caupin, S. Balibar, and H. J. Maris, Limits of metastability of liquid helium, [Phys. B: Condens. Matter \*\*329\*\*, 356 \(2003\)](#).